

**Ab initio description of the thermoelectric properties of heterostructures  
in the diffusive limit of transport**

Hinsche, N. F.; Rittweger, F.; Hölzer, M.; Zahn, P.; Ernst, A.; Mertig, I.;

Originally published:

March 2016

**Physica Status Solidi (A) 213(2016), 672-683**

DOI: <https://doi.org/10.1002/pssa.201532410>

Perma-Link to Publication Repository of HZDR:

<https://www.hzdr.de/publications/Publ-24008>

Release of the secondary publication  
on the basis of the German Copyright Law § 38 Section 4.

# *Ab initio* description of the thermoelectric properties of heterostructures in the diffusive limit of transport

Nicki F. Hinsche<sup>\*,1</sup>, Florian Rittweger<sup>1,2</sup>, Martin Hölzer<sup>1</sup>, Peter Zahn<sup>3</sup>, Arthur Ernst<sup>2</sup> and Ingrid Mertig<sup>1,2</sup>

<sup>1</sup> Institut für Physik, Martin-Luther-Universität Halle-Wittenberg, 06099 Halle/Saale, Germany

<sup>2</sup> Max-Planck-Institut für Mikrostrukturphysik, Weinberg 2, 06120 Halle, Germany

<sup>3</sup> Helmholtz-Zentrum Dresden - Rossendorf, Bautzner Landstr. 400, 01328 Dresden, Germany

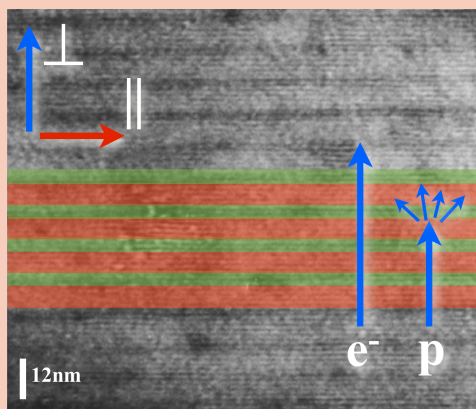
Received XXXX, revised XXXX, accepted XXXX

Published online XXXX

**Key words:** *Ab initio*, Boltzmann transport, thermoelectric transport, heterostructures, strain, chalcogenides, silicon

\* Corresponding author: e-mail nicki.hinsche@physik.uni-halle.de

The scope of this reviewing article is to present the recent progress in the understanding of the microscopic origin of thermoelectric transport in semiconducting heterostructures and to identify and elucidate mechanisms which could lead to enhanced thermoelectric conversion efficiency. Based on first-principles calculations a consistent and convenient method is presented to fully describe the thermoelectric properties in the diffusive limit of transport for bulk systems and their associated heterostructures. While fundamentals of the functionality of phonon-blocking and electron-transmitting superlattices could be unveiled, we provide also distinct analysis and ideas for thermoelectric enhancement for two archetypical thermoelectric heterostructures based on  $\text{Bi}_2\text{Te}_3/\text{Sb}_2\text{Te}_3$  and  $\text{Si}/\text{Ge}$ . A focus was on the influence of bulk and interfacial strain, varying charge carrier concentration, temperature and superlattice periods on the thermoelectric transport properties.



Transmission electron micrograph of a 10Å/50Å  $\text{Bi}_2\text{Te}_3/\text{Sb}_2\text{Te}_3$  superlattice. Red and green areas highlight the layered structure. For optimal cross-plane transport ( $\perp$ ) phonons (p) are expected to be scattered at the interfaces, while electrons ( $e^-$ ) transmit without losses.

Copyright line will be provided by the publisher

**1 Introduction** A major goal in optimizing thermoelectric nanomaterials is to strengthen the theoretical understanding of anisotropic thermoelectric (TE) transport in semiconducting phonon-blocking and electron-transmitting heterostructures and to elucidate details of the electronic structure, which could be the origin of high thermoelectric conversion efficiency in the cross-

plane transport direction of these systems. Motivated by state-of-the-art experiments, superlattices (SL) based on  $\text{Bi}_2\text{Te}_3/\text{Sb}_2\text{Te}_3$  or  $\text{Si}/\text{Ge}$  were of major interest. For this purpose, *ab initio* calculations based on KORRINGA-KOHN-ROSTOKER [1] and plane-wave methods [2,3] were carried out. Here, it was accounted for all important relativistic effects, by solving the DIRAC equation. The

Copyright line will be provided by the publisher

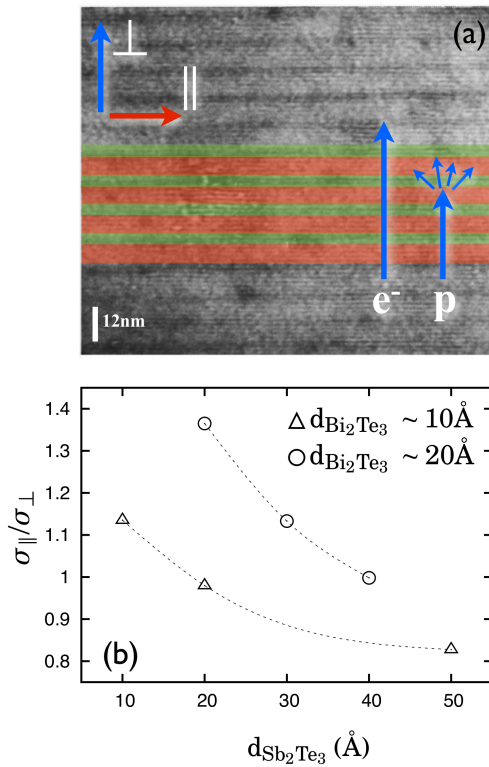


**Figure 1** (a) TEM of a  $10\text{\AA}/50\text{\AA}$   $\text{Bi}_2\text{Te}_3/\text{Sb}_2\text{Te}_3$ -SL. Red and green areas highlight the layered structure. For optimum cross-plane transport ( $\perp$ ) phonons (p) are expected to be scattered at the interfaces, while electrons ( $e^-$ ) transmit without losses. In the in-plane direction ( $\parallel$ ) quantum confinement effects for electrons are expected. Figure modified from [4]. (b) Experimental electrical conductivity anisotropy for different  $\text{Bi}_2\text{Te}_3/\text{Sb}_2\text{Te}_3$ -SL. Cross-plane transport was found most preferable for a  $10\text{\AA}/50\text{\AA}$   $\text{Bi}_2\text{Te}_3/\text{Sb}_2\text{Te}_3$ -SL. Data from [5].

macroscopic TE transport properties were then described by a linearized BOLTZMANN equation. This review aims to present the main results of the finalized project.

**1.1 Phonon-blocking and electron-transmitting superlattices** The very sophisticated TE concept of phonon-blocking and electron-transmitting superlattices (PBET-SL) combines the phonon-glass-electron-crystal (PGEC) approach [6,7] and the idea of quantum confinement in low-dimensional systems [8,9]. Made available by state-of-the-art heteroepitaxy [10–15], SL consist of alternating thin layers of different materials stacked periodically. Most prominent applications of TE SL are  $\text{Bi}_2\text{Te}_3/\text{Sb}_2\text{Te}_3$  [16,17,5,13,14],  $\text{Si}/\text{Ge}$  [18–20] and SL based on  $\text{PbTe}$  and  $\text{PbSe}$  [21–26]. Other SL based on  $\text{Bi}/\text{Sb}$  [27] or skutterudites [28] showed negligible or only small enhancements of the TE efficiency.

Even though being inspired by the approaches of a PGEC and the concept of quantum confinement in lower dimensions, the *ansatz* of a PBET-SL is very different. First, their quantum confinement differ from each other. In low-dimensional 1D and 2D nanostructures proposed by HICKS & DRESSELHAUS, the transport is usually perpendicular to the confinement, i.e. in the basal plane of the SL, and can be assumed nearly free-electron-like. In a PBET-SL the thermal gradient is preferably applied parallel to the confinement, i.e. electron and phonon transport occur in cross-plane direction of the superlattice. The latter is emphasized in Fig. 1(a).

With no obvious enhancement of the cross-plane electronic transport to be expected due to quantum confinement effects, the desired increase in  $ZT$  has to stem entirely from a distinct reduction of the cross-plane lattice thermal conductivity  $\kappa_{\text{ph},\perp}$ . Indeed, exceptionally low thermal conductivities were found for PBET-SL [18,29–31,22,32]. Venkatasubramanian *et al.* reported  $\kappa_{\text{ph},\perp} = 0.22 \text{ W/mK}$  for  $\text{Bi}_2\text{Te}_3/\text{Sb}_2\text{Te}_3$  SL with a period of  $50\text{\AA}$ , which is about five times smaller than the bulk values and significantly below the alloy limit [29]. Those values add up to the lowest room-temperature thermal conductivities in crystalline materials being reported so far.

The physical reason for the minimized cross-plane thermal conductivity is still under intense debate applying two model pictures [10]. In the first, the phonons are expected to be quasiparticles that are scattered specularly or diffusively at the interfaces [33]. Experimental results from TOUZELBAEV are able to support this picture, as increasing interface roughness leads to decreased lattice thermal conductivity [12]. In the second, the phonons are expected to behave as coherent waves across the interfaces. Reduction of the thermal conductivity then comes purely from band structure effects, like Brillouin-zone (BZ) downfolding, which leads to decreased phonon group velocities and thermal conductivities [34,35]. This picture alone is not sufficient to explain the magnitude of the thermal conductivity reduction perpendicular to the film plane, and it fails completely to explain the observed in-plane thermal conductivity reduction [10]. Venkatasubramanian *et al.* proposed that coherent backscattering of phonons at *mirror-like* interfaces could lead to standing phonon waves which do not contribute to the thermal transport [29]. Depending on the SL period  $l$ , this leads to a localization of certain phonon modes with wavelength  $\lambda \leq l/2$  [29]. The aim of SL engineering is to choose the SL period in such a way that low-frequency acoustic modes are localized and  $\kappa_{\text{ph}}$  most probably becomes diminished.

At the best, a PBET-SL shows power factors similar to that of the bulk, albeit at different optimal carrier concentrations. As will be shown these assumptions are *per se* rather optimistic but accessible under specific conditions. Summing up, TE transport in the cross-plane direction of SL shows the highest numbers for the figure of merit so far.  $ZT = 1.5$  and  $2.4$  were predicted for  $n$ -type and  $p$ -

type  $\text{Bi}_2\text{Te}_3/\text{Sb}_2\text{Te}_3$  SLs at room temperature [4], while  $ZT = 1.6 - 3.5$  was reported for  $n$ -type  $\text{PbSeTe}$ -based SL at  $T = 300 - 600$  K [21–23]<sup>1</sup>.

**2 Transport Theory** Owing knowledge to the microscopic electronic structure of a material by means of density functional theory (DFT), the macroscopic TE transport properties can be obtained within the BOLTZMANN transport theory [37,38]. Hereinafter, the generalized electronic transport coefficients will be derived in detail by solving a linearized BOLTZMANN equation. Hence, the thermoelectric transport processes can be written and discussed by means of generalized forces and fluxes. Analogously solving the BOLTZMANN equation for the phonon distribution function yields access to the lattice thermal conductivity.

**2.1 Linearized BOLTZMANN equation and relaxation time approximation** We restrict the following considerations to a temperature gradient  $\nabla T$ , and a time-independent external electric field  $\mathcal{E}$ . Applying weak external fields, one can expect that a system in a steady state will only slightly vary from its equilibrium distribution. Therefore, it is suitable that the electronic state occupation function  $f_k$  in the steady state can be split into the equilibrium contribution  $f_k^0$  given by the FERMI-DIRAC distribution at chemical potential  $\mu$  and temperature  $T$  and a modest perturbation  $g_k$ :

$$f_k = f_k^0 + g_k \quad \text{with} \quad f_k^0 = \frac{1}{e^{(E_k - \mu)/k_B T} + 1} . \quad (1)$$

The semiclassical equation of motion for the position  $\mathbf{r}$  and the wave vector  $\mathbf{k}$  can be used to express the collision integral as the temporal change of the  $f_k$  by the action of the external electric field  $\mathcal{E}$  [37]. Supposing only weak fields and small temperature gradients, a linearized BOLTZMANN equation is obtained. Assuming additionally that the collision integral is proportional to the perturbation  $g_k$  divided by the relaxation time  $\tau_k$ , the solution of the BOLTZMANN equation in relaxation time approximation (RTA) can be written as

$$g_k = \tau_k \mathbf{v}_k \left[ |e| \mathcal{E} + \frac{E_k - \mu}{T} \nabla T \right] \frac{\partial f_k^0}{\partial E} . \quad (2)$$

The derivative  $\frac{\partial f_k^0}{\partial E}$  of the FERMI-DIRAC distribution function indicates that only electrons within an energy shell in the order of  $k_B T$  around the FERMI surface can react to the external forces. Here, unoccupied states are in their vicinity and are redistributed in  $\mathbf{k}$ -space.

**2.2 Transport coefficients** While it has been discussed in the last section how a weak electric field and a thermal gradient modify the population of electronic states,

<sup>1</sup> Some of the measurements for the  $\text{PbSeTe}$ -based SL have been corrected after publication by the authors [36]. The maximum value of  $ZT = 3.5$  is highly unlikely,  $ZT > 1$  is expected for all the samples.

one may infer which electrical and heat currents  $\mathbf{j}$  and  $\mathbf{Q}$  will exist in the steady state. Taking into account that  $f_k = f_k^0 + g_k$  and that there is no spontaneous net current flow in equilibrium, only  $g_k$  of the perturbed occupation function  $f_k$  causes a current flow. With Eq. (2) the currents can be expressed by the generalized conductivity moments with the moment's order  $n$

$$\mathcal{L}_{(\parallel, \perp)}^{(n)}(\mu, T) = \int dE \Sigma_{(\parallel, \perp)}(E) \cdot (E - \mu)^n \left( -\frac{\partial f_k^0(\mu, T)}{\partial E} \right)_{E_k=E} , \quad (3)$$

involving integrations over surfaces of constant electron energy  $E$  in reciprocal space:

$$\Sigma_{(\parallel, \perp)}(E) = \frac{1}{\hbar(2\pi)^3} \oint_{E_k=E} \frac{dS}{|\mathbf{v}_k|} \tau_k (\mathbf{v}_{k,(\parallel, \perp)})^2 . \quad (5)$$

The directional indices ' $\parallel$ ' and ' $\perp$ ' refer to the transport properties within and perpendicular to the basal plane of the layered systems considered here. In an isotropic or cubic system this directional dependency disappears.

$\Sigma_{(\parallel, \perp)}(E)$  is the zeroth moment at vanishing temperature and coincides with the transport distribution function (TDF)  $\Sigma_{(\parallel, \perp)}(E) \equiv \mathcal{L}_{(\parallel, \perp)}^{(0)}(E, T = 0)$  as introduced to thermoelectrics by MAHAN & SOFO [39].

Using the definitions above, the electric and heat current densities can be expressed in terms of the generalized conductivity moments

$$\mathbf{j} = e^2 \mathcal{L}^{(0)} \mathcal{E} - \frac{e}{T} \mathcal{L}^{(1)} \nabla T , \quad (6)$$

$$\mathbf{Q} = e \mathcal{L}^{(1)} \mathcal{E} - \frac{1}{T} \mathcal{L}^{(2)} \nabla T . \quad (7)$$

Depending on the boundary conditions certain transport coefficients can be deduced connecting acting fields and resulting quantities.

At a constant temperature, an electric current  $\mathbf{j}$  flows in the material in response to an applied external electric field  $\mathcal{E}$ . Comparing Eq. (6) with OHM's law one obtains

$$\mathbf{j} = \sigma \mathcal{E} \quad \text{with} \quad \sigma = e^2 \mathcal{L}^{(0)} , \quad (8)$$

where  $\sigma$  is the electric conductivity tensor. Here,  $\sigma_{xx,zz} = \sigma_{\parallel, \perp}$  correspond to the diagonal components within and perpendicular to the basal plane, respectively.

Assuming an electrical open circuit  $\mathbf{j} = 0$  and applying a steady thermal gradient along the sample, the resulting electric field  $\mathcal{E} = S \nabla T$  is given by

$$\mathcal{E} = \frac{1}{eT} \frac{\mathcal{L}^{(1)}}{\mathcal{L}^{(0)}} \nabla T \quad \text{with} \quad S = \frac{1}{eT} \frac{\mathcal{L}^{(1)}}{\mathcal{L}^{(0)}} . \quad (9)$$

$S$  is called the SEEBECK coefficient or thermopower.

Combining the thermopower in Eq. (9) with the electrical conductivity in Eq. (8), the thermoelectric power factor reads

$$\text{PF} = \sigma S^2 = \frac{1}{T^2} \frac{(\mathcal{L}^{(1)})^2}{\mathcal{L}^{(0)}}, \quad (10)$$

which is the electrical power throughput of a material at a given temperature difference. The power factor strongly depends on the charge carrier concentration of the thermoelectric material and should be optimized to maximize the figure of merit  $ZT$ .

The electronic part to the total thermal conductivity accounts to

$$\kappa_{\text{el},(\perp,\parallel)} = \frac{1}{T} (\mathcal{L}_{\perp,\parallel}^{(2)}(\mu, T) - \frac{(\mathcal{L}_{\perp,\parallel}^{(1)}(\mu, T))^2}{\mathcal{L}_{\perp,\parallel}^{(0)}(\mu, T)}), \quad (11)$$

with the heat current  $\mathbf{Q}_{\perp,\parallel} = -\kappa_{\text{el},\perp,\parallel} \nabla T$ .

The second term in Eq. (11) gives corrections due to the Peltier heat flow that occur when bipolar conduction is present [42,45]. With Eqs. (9) and (11) and the abbreviation  $\kappa_{\text{el},\perp,\parallel}^0 = \frac{1}{T} \mathcal{L}_{\perp,\parallel}^{(2)}(\mu, T)$  [39], the LORENZ function reads as

$$L_{\perp,\parallel} = \kappa_{\text{el},(\perp,\parallel)} \cdot (\sigma_{\perp,\parallel} \cdot T)^{-1}, \quad (12)$$

$$L_{\perp,\parallel} = \frac{\kappa_{\text{el},(\perp,\parallel)}^0}{\sigma_{\perp,\parallel} T} - S_{\perp,\parallel}^2. \quad (13)$$

Clearly, in the low temperature regime the LORENZ function  $L$  consists of a constant term and a negative term of order  $T^2$ . A detailed analysis for the LORENZ function of the  $\text{Bi}_2\text{Te}_3/\text{Sb}_2\text{Te}_3$  SL was given in Refs. [46,44], where the directional anisotropy of  $L$  was found to be an intricate function of the SL period. Results for the anisotropic bulk LORENZ function of  $\text{Bi}_2\text{Te}_3$  are shown in Fig. 2(c).

In the most realistic case one has to assume the presence of an electric field, a thermal gradient, and an electric current  $\mathbf{j}$ , simultaneously. Thus, eliminating the electric field, the general heat flux is rewritten as

$$\mathbf{Q} = \Pi \mathbf{j} - \kappa_{\text{el}} \nabla T, \quad (14)$$

introducing the Peltier coefficient  $\Pi = ST$ . Calculating the divergence of the heat flux and rearranging one obtains [47]

$$T \nabla S \cdot \mathbf{j} = T \mathbf{j} \cdot \nabla \left( \frac{\Pi}{T} \right) = \mathbf{j} \cdot (\nabla(ST) - S \nabla T). \quad (15)$$

Thereby, a classical separation of the Peltier and THOMSON contribution is artificial, as both effects ground on the gradient of the thermopower [47]. This can be either the temperature driven gradient  $S \nabla T$ , or the spatially driven gradient  $(\nabla S) T$ . At isothermal conditions, Eq. (15) yields

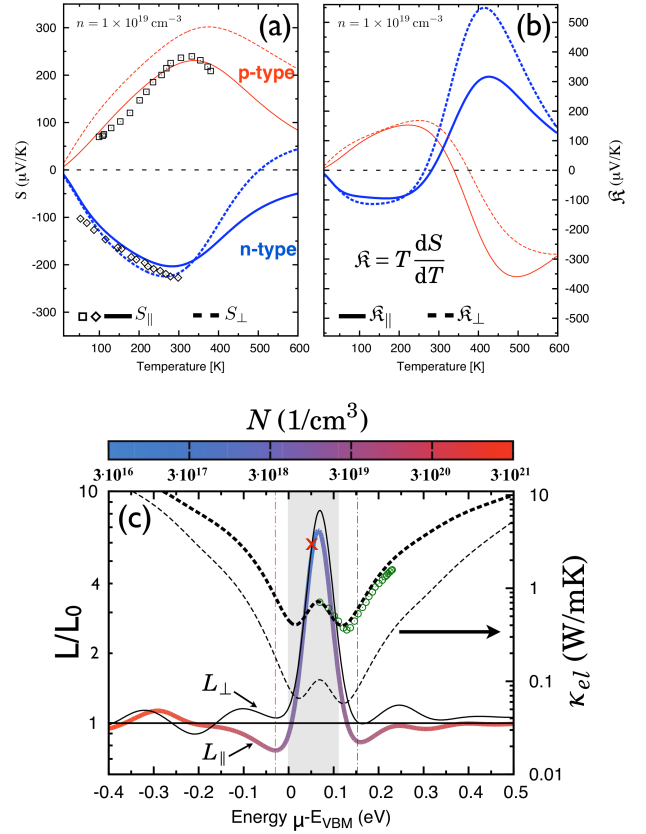


**Figure 2** (a) Anisotropic thermopower for bulk  $\text{Bi}_2\text{Te}_3$ . Electron doping refers to the blue (thick) lines, while red (thin) lines refer to hole doping. Solid lines show the in-plane part  $S_{\parallel}$  of the thermopower, while dashed lines show the cross-plane part  $S_{\perp}$ . The extrinsic charge carrier concentration was fixed to  $N = 1 \times 10^{19} \text{ cm}^{-3}$ . Experimental data (squares, diamonds) from Ref. [40,41] are given for comparison. (b) THOMSON coefficient for  $\text{Bi}_2\text{Te}_3$  in the same representation as done for (a). (c) LORENZ function  $L$  (ref. to left scale) and electronic contribution  $\kappa_{\text{el}}$  to the total thermal conductivity (ref. to the right scale) in dependence on position of the chemical potential  $\mu$  for bulk  $\text{Bi}_2\text{Te}_3$ . Shown are the in-plane (thick lines) and cross-plane (thin lines) transport direction. Superimposed onto the LORENZ function in the in-plane direction is a color code referring to the charge carrier concentration. The red cross points out the change from  $n$  to  $p$  doping. Thin vertical dash-dotted lines emphasize the position of the chemical potential for a charge carrier concentration of  $N = 3 \times 10^{19} \text{ cm}^{-3}$  under  $n$  and  $p$  doping (blue and red line), respectively. The conduction band maximum (CBM) is located at  $0.105 \text{ eV}$ . Green open circles show experimental values from Ref. [42] for  $\kappa_{\text{el},\parallel}$  for an  $n$ -type  $\text{Bi}_2\text{Te}_3$  single crystal. The temperature is fixed to  $300 \text{ K}$  and the LORENZ function is related to the classical metallic limit  $L_0 = 2.44 \times 10^{-8} \text{ W}\Omega/\text{K}^2$ . Adapted with permission from Refs. [43,44], Copyright (2011,2012) APS.

the pure Peltier effect as  $\mathbf{j} \cdot \nabla (ST)$ . For a homogenous material under a temperature gradient,

$$\mathbf{j} \cdot (\nabla \Pi - S \nabla T) = \mathbf{j} \cdot \left( \frac{d\Pi}{dT} - S \right) \nabla T = \mathfrak{R} \mathbf{j} \nabla T \quad (16)$$

holds. Here,  $\mathfrak{R}$  is introduced as THOMSON coefficient of a material, connected with a THOMSON heat per volume  $\mathfrak{R} \mathbf{j} \nabla T$  [48]. The THOMSON coefficient is a measure for the heat absorbed or emitted when the current  $\mathbf{j}$  flows in the one or other direction of a temperature gradient. In metals, the THOMSON coefficient compares to the magnitude of the thermopower and is rather small with values below a few  $\mu\text{V}/\text{K}$ . Hence, the related heat is only of minor relevance. In non-degenerate semiconductors, the thermopower  $S$  can take rather large values of above several hundreds  $\mu\text{V}/\text{K}$ . Additionally, the dependence of  $S$  on the temperature is strongly non-monotonic, which favours enhanced values of the derivative  $\frac{dS}{dT}$ . To give some insight on this feature, in Fig. 2(a),(b) the temperature-dependent anisotropic thermopower and the related THOMSON coefficient are shown for bulk  $\text{Bi}_2\text{Te}_3$  for an electron and hole doping of  $N = 1 \times 10^{19} \text{ cm}^{-3}$ , respectively. Here, at operating temperatures between  $T = 350 - 400 \text{ K}$  an average THOMSON coefficient of about  $490 \mu\text{V}/\text{K}$ , can be stated under electron doping in the cross-plane transport direction. This number is far below the optimal value of  $\mathfrak{R} = 1500 \mu\text{V}/\text{K}$ , which was suggested for optimally graded materials based on  $\text{Bi}_x(\text{SbTe})_{(1-x)}$  [49]. This magnitude of the THOMSON coefficient could be even more enhanced for wide band gap semiconductors ( $E_g > 1 \text{ eV}$ ) at very low charge carrier concentrations of  $N \leq 1 \times 10^{14} \text{ cm}^{-3}$ . At the same time, bipolar conduction is suppressed and electrical conductivity is small. Consequently, the absorbed or generated heat  $\mathfrak{R} \mathbf{j} \nabla T$  is tiny and the THOMSON effect is ineligible for cooling applications [48].

Nevertheless, beside the need of sophisticated techniques to measure  $\mathfrak{R}$ , knowledge and controlling of the THOMSON coefficient could e.g. lead to a significant reduction of the programming current in phase-change memory devices [50]. Moreover a large  $\mathfrak{R}$  in a broad temperature range could lead to a new kind of thermoelectric coolers based on the THOMSON effect. These would enable solid-state cooling to cryogenic temperatures [48, 49].

**2.3 Phonon transport properties** BOLTZMANN'S transport theory can also be applied to phonons by simply accounting for the Boson occupation function

$$n_\omega^0 = \frac{1}{e^{\hbar\omega_q/k_B T} - 1} \quad , \quad (17)$$

where  $\omega_q$  is the phonon frequency dispersion, and  $q$  is a short-hand notation for the wave vector and the phonon branch. Equivalent to the path described in section 2.1, one can derive the linearized phonon BOLTZMANN transport equation (PBTE) in RTA [51, 37, 52, 53]. Similar to Eq. (5), the phonon thermal conductivity  $\kappa_{ph,(\parallel,\perp)}(T)$  can be cal-

culated as

$$\kappa_{ph}(T) = \int d\omega \Sigma_{ph}(\omega) C_V(\omega, T) \quad , \quad (18)$$

including integrations over surfaces of constant phonon frequency  $\omega$ ,

$$\Sigma_{ph,(\parallel,\perp)}(\omega) = \frac{1}{8\pi^3} \oint_{\omega_q=\omega} \frac{dS}{|v_q|} \tau_q v_{q,(\parallel,\perp)}^2 \quad . \quad (19)$$

These properties are analogous to the electronic case in Eq. (5) and include the phonon density of states (PDOS)  $\mathcal{F}(\omega)$ . Within, the specific thermal heat at constant volume and temperature  $T$  will be defined as

$$C_V(\omega, T) = \frac{(\hbar\omega)^2}{k_B T^2} n_\omega^0 (n_\omega^0 + 1) \quad . \quad (20)$$

Ingredients of the kernel Eq. (19) are the phonon frequency dispersion (cf. Fig. 3 (a)) and the corresponding phonon density of states (PDOS), which has been calculated using either plane wave codes [3, 56, 2] or a phonon Green function method [57], respectively. Accurate force calculations for  $\text{Bi}_2\text{Te}_3$  supercells of 40 atoms have been performed to construct the dynamical matrix and thus the phonon frequencies and the eigenvectors of the vibrational modes. Fig. 3 (b) shows the calculated (solid line) and measured (circles, [54]) total PDOS of bulk  $\text{Bi}_2\text{Te}_3$ . The calculated data has been convoluted with a Gaussian of width 1.5 meV (experimental resolution) for better comparability. The overall correspondence between theory and experiment is very convincing, with the exception of the acoustic bandwidth being overestimated by the calculations. The main features above 7 meV are in good agreement. Comparing to other experimental methods, namely ultrasonic studies [58] and recent synchrotron radiation measurements by Bessas et al. [55], even the acoustic branch is in very good agreement with experiments (see below). The coloured lines in panel (b) show the element-resolved partial PDOS of Bi and Te, respectively. As pointed out, the locally resolved contributions to the acoustic branches and the lower optical modes below 10 meV are dominated by Bi, whereas the higher energetic parts of the vibronic spectrum are dominated by Te oscillations. Green squares denote the Te-PDOS measured using Mössbauer spectroscopy [55]. These experiments have been performed with higher energetic resolution compared to the neutron scattering reference data and show a better agreement with theoretical data in the acoustic region. Evaluating the directional PDOS sheds some light on the main components of the optical frequencies. As an example, Fig. 3 (c) shows the in-plane and out-of plane components of the partial PDOS of the  $\text{Te}_1$  as well as the  $\text{Te}_2$  site. The peaks of the PDOS at 10 meV and 12 meV are mainly originating from the respective transverse and longitudinal oscillations of these atoms perpendicular to the  $c$  axis. In

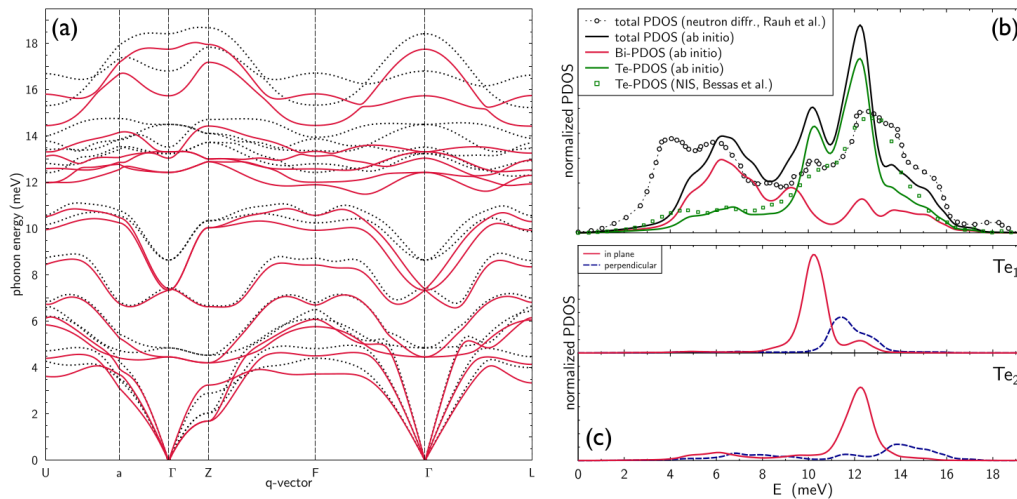


**Figure 3** (a) Phonon dispersion of rhombohedral bulk  $\text{Bi}_2\text{Te}_3$  obtained by a DFT supercell calculation within a non-relativistic (black-dashed lines) and full-relativistic (solid red lines) approach. (b) Partial and total phonon DOS of bulk  $\text{Bi}_2\text{Te}_3$ . Circles represent the corresponding neutron scattering measurements[54] and squares denote results for the Te partial PDOS obtained by Mössbauer spectroscopy measurements[55]. (c) Directionally and spatially resolved phonon DOS for the two inequivalent Te sites. Solid lines show the in-plane components of the PDOS and dashed lines show the component parallel to  $z$  direction. The theoretical data in panels (b) and (c) have been convoluted with a Gaussian for better comparability with the measured curve.

particular the directional PDOS of  $\text{Te}_2$  reflects the strong bonding within the Te layers, compared to the relatively weak Van-der-Waals bonding between neighbouring Te layers.

The developed methods allow an accurate calculation of vibrational modes for state-of-the art thermoelectrics, i.e.  $\text{Bi}_2\text{Te}_3$ , from first principles which are in good agreement with experimental data. A very challenging task to obtain the *ab initio* lattice thermal conductivity  $\kappa_{\text{ph}}$  is still the evaluation of the phonon-phonon coupling matrices and corresponding relaxation times  $\tau_q$ . In contrast to the electronic case a constant  $\tau_q$  fails completely. In the most simplified case, the phonon mean free paths  $\Lambda(\mathbf{q})$  have at least to be modeled by empirical approaches based on DE-BYE-models neglecting the phonon dispersion relation, and introducing parameters to treat different scattering mechanisms [59,60].

Today, sophisticated methodology [61] allows for the solution of the PBTE and possible access to the phonon mean free paths based on *ab initio* calculations. When the dominant scattering events are two- and three-phonon processes the first principle calculation of the second- and third-order interatomic force constants is sufficient to evaluate the phonon spectra and the three-phonon scattering rates, respectively. Recently great effort was done to numerically represent three phonon processes by the calculation of anharmonic force constants within supercell and density functional perturbation schemes (DFPT) schemes [62–64].

With the three-phonon scattering rates being indirectly proportional to the phonon relaxation times  $\tau_q$ , the PBTE can be solved in the relaxation time approximation (RTA), i.e.  $\Lambda(\mathbf{q}) = \tau_q \mathbf{v}(\mathbf{q})$ . While the RTA is accounting only for non-momentum-conserving Umklapp processes the theoretical RTA results most often reproduce the experimental data of  $\kappa_{\text{ph}}$  within 10% at room-temperature [65,63,66]. Within the RTA *ab initio* calculations for the lattice thermal conductivity of bulk  $\text{Bi}_2\text{Te}_3$ [67], Si and Ge [64] and even Si/Ge heterostructures [68,69] have been performed successfully.

While being omitted within the RTA, momentum-conserving normal three-phonon processes can play a significant role for materials with very high  $\kappa_{\text{ph}}$ , e.g. diamond or graphene. Here, the PBTE has to be solved iteratively to self-consistency and gives the most accurate results for  $\Lambda(\mathbf{q})$ . This approach has been implemented very recently [70].

### 3 Results for thermoelectric heterostructures

**3.1  $\text{Bi}_2\text{Te}_3/\text{Sb}_2\text{Te}_3$  heterostructures** The chalcogenides  $\text{Bi}_2\text{Te}_3$  and  $\text{Sb}_2\text{Te}_3$  and their solid solutions dominated efficient bulk thermoelectrics with  $ZT \approx 0.5 - 1$  in the last fifty years [71–73]. The intrinsic layered  $\text{Bi}_2\text{Te}_3$  and  $\text{Sb}_2\text{Te}_3$  show large anisotropies in their crystal structure and their thermoelectric transport properties. At first glance, the anisotropic electronic structure of both materials was studied in detail [74]. The band structure's topology is very complex, and strong spin-orbit-coupling

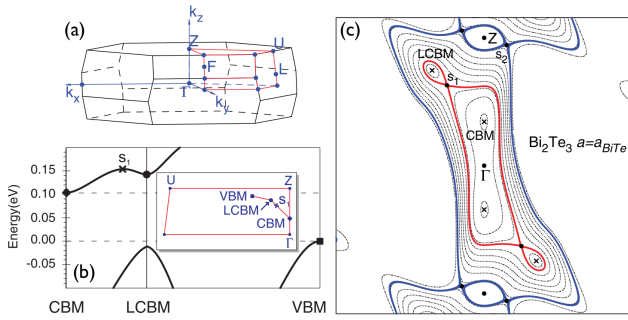


**Figure 4** (Color online) (a) Brillouin zone of the rhombohedral lattice. (b) band structure of unstrained bulk  $\text{Bi}_2\text{Te}_3$  near the band gap along the lines shown in the inset. (c) Contour plot of  $E(\mathbf{k})$  at the experimental lattice constant in the plane ( $\Gamma Z U$ ) for  $\text{Bi}_2\text{Te}_3$ . 10 isolines for  $E - E_{\text{CBM}}$  at 0 to 0.19 eV with a constant increment (dotted); additionally, two isolines at  $E - E_{\text{CBM}} = 0.05$  eV and  $E - E_{\text{CBM}} = 0.17$  eV with the saddle points  $s_1$  and  $s_2$ , respectively (bold). The positions of the conduction band minimum (CBM) and the local conduction band minimum (LCBM) are marked with crosses. Adapted with permission from Ref. [74], Copyright (2011) APS.

effects dictate the formation of the band edges. To give an example, as shown in Fig. 4(b) and (c), the conduction band minimum (CBM) of  $\text{Bi}_2\text{Te}_3$  was found to consist of two valleys, in contrast to the six-valley model proposed by DRABBLE & WOLFE [75]. However, at slightly increased band occupation of about  $N = 3 \times 10^{19} \text{ cm}^{-3}$ , additional local CBM off the high symmetry lines are occupied, forming the expected six valleys in reciprocal space.

Specific details of the band structures topology, like saddle points, were furthermore found to be direct sources of extrema of the electrical conductivity anisotropy [74]. In Ref. [43] it is shown that the anisotropy of the electrical conductivity surpasses the experimental findings for  $\text{Bi}_2\text{Te}_3$ , but not for  $\text{Sb}_2\text{Te}_3$ , implying anisotropic scattering effects in the first. By detailed convergence and model studies it was shown, that different numerical methods for the determination of the electrical conductivity anisotropy can give results closer to experiment, hiding the evidence for possible anisotropic scattering effects [76]. Contrary to earlier experimental assumptions [77,78], the anisotropy of the thermopower of both tellurides stems to a large amount, probably entirely, from band structure effects, more precisely from a distinct anisotropy of the TDF (cf. Ref. [43]).

The application of interfacial strain in epitaxially grown  $\text{Bi}_2\text{Te}_3$  and  $\text{Sb}_2\text{Te}_3$  in order to optimize the TE transport properties was found to be unsatisfying [43]. Due to compensation effects of the strain-dependent thermopower and electrical conductivity, the related power factor decreases under applied compressive in-plane strain for

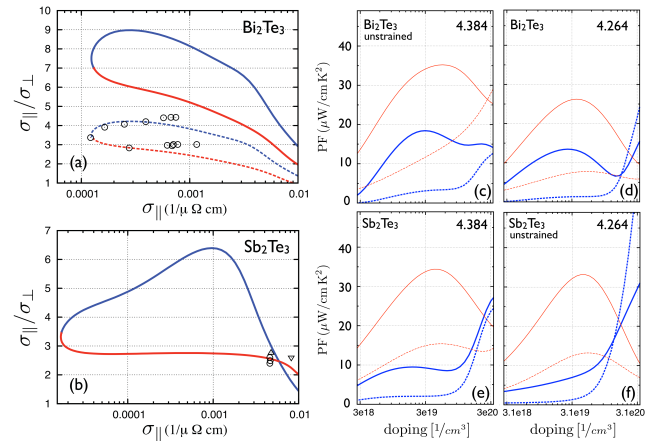


**Figure 5** Calculated electrical conductivity anisotropy at 300 K of bulk (a)  $\text{Bi}_2\text{Te}_3$  and (b)  $\text{Sb}_2\text{Te}_3$ . Electron doping refers to blue lines, while red lines refer to hole doping. The dashed lines in panel (a) present the ratio obtained with an anisotropic relaxation time  $\tau_{\parallel}/\tau_{\perp} = 0.47$ , while all other results are obtained with an isotropic relaxation time ( $\tau_{\parallel} = 11$  fs (12 fs) for  $\text{Bi}_2\text{Te}_3$  ( $\text{Sb}_2\text{Te}_3$ )). Experimental data (circles and triangles) are given for comparison (further details in [43]). (c)-(f) In-plane (solid lines) and cross-plane (dashed lines) doping-dependent powerfactor at 300K for (c)  $\text{Bi}_2\text{Te}_3$  in the  $\text{Bi}_2\text{Te}_3$  structure, (d)  $\text{Bi}_2\text{Te}_3$  in the  $\text{Sb}_2\text{Te}_3$  structure, (e)  $\text{Sb}_2\text{Te}_3$  in the  $\text{Bi}_2\text{Te}_3$  structure and (f)  $\text{Sb}_2\text{Te}_3$  in the  $\text{Sb}_2\text{Te}_3$  structure. Electron (hole) doping is presented as blue thick (red thin) line. The lattice constants of unstrained bulk  $\text{Bi}_2\text{Te}_3$  and  $\text{Sb}_2\text{Te}_3$  are 4.384 Å and 4.264 Å, respectively. Adapted with permission from Ref. [43], Copyright (2011) APS.

$\text{Bi}_2\text{Te}_3$ , while being stable for tensile strained  $\text{Sb}_2\text{Te}_3$  (cf. Fig. 5(c)-(f)). Thus, growing  $\text{Bi}_2\text{Te}_3/\text{Sb}_2\text{Te}_3$ -SLs, a substrate favouring  $\text{Bi}_2\text{Te}_3$  should be chosen for TE applications, because the transport properties of  $\text{Sb}_2\text{Te}_3$  are much more robust under applied strain.

In 2001, Venkatasubramanian *et al.* made considerable contributions to the field of chalcogenide TE's. These authors introduced the concept of a PBET-SL [11,5] and hence found the cross-plane lattice thermal conductivity to be drastically reduced below the alloy limit [16,29]. Furthermore, it was argued that the electrical conductivity anisotropy  $\sigma_{\parallel}/\sigma_{\perp}$  is a function of the SL period and reduces to values smaller than found for bulk, clearly preferring the cross-plane transport  $\sigma_{\parallel}/\sigma_{\perp} \leq 1$  (cf. Fig. 1) for some heterostructures. Both experimental findings added up to the highest values for the figure of merit so far:  $ZT = 2.4$  for a *p*-type  $\text{Bi}_2\text{Te}_3/\text{Sb}_2\text{Te}_3$  SL and  $ZT = 1.5$  for a *n*-type  $\text{Bi}_2\text{Te}_3/\text{Bi}_2\text{Te}_{2.83}\text{Se}_{0.17}$  at room temperature.

The findings of  $\sigma_{\parallel}/\sigma_{\perp} \leq 1$  are contrary to expectations, as  $\sigma_{\parallel}/\sigma_{\perp} \sim 2.5 - 5.5$  for bulk  $\text{Sb}_2\text{Te}_3$  and  $\text{Bi}_2\text{Te}_3$  (cf. Fig. 5(a),(b) and [43]). Further carrier confinement in the cross-plane direction due to the heterostructure should be

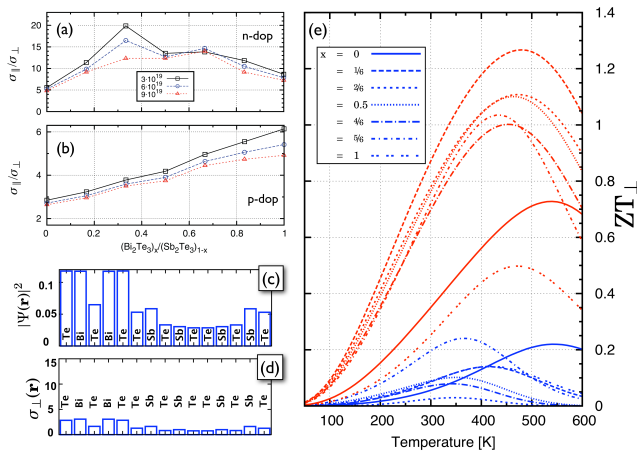


**Figure 6** (a) and (b) Directional anisotropies of the electrical conductivity for  $(\text{Bi}_2\text{Te}_3)_x/(\text{Sb}_2\text{Te}_3)_{1-x}$  SLs in dependence on the superlattice period at 300 K. Results for three different charge carrier concentrations (in units of  $\text{cm}^{-3}$ ) are compared, for (a) electron doping and (b) hole doping. (c) Site-resolved probability amplitude for a  $(\text{Bi}_2\text{Te}_3)_x/(\text{Sb}_2\text{Te}_3)_{1-x}$  SLs with  $x = 2/6$ . In the same manner, the site-resolved cross-plane electrical conductivity [in units of  $(\text{cm})^{-1}$ ] is shown. The temperature is fixed at 300 K, the charge carrier concentration is  $N = 3 \times 10^{19} \text{ cm}^{-3}$ . (e) Cross-plane figure of merit for different  $(\text{Bi}_2\text{Te}_3)_x/(\text{Sb}_2\text{Te}_3)_{1-x}$  SLs at varying temperature and fixed charge carrier concentration of  $N = 3 \times 10^{19} \text{ cm}^{-3}$ . Here, red and blue lines constitute *p*- and *n*-doping, respectively. Here, the electronic part  $\kappa_{el}$  was calculated, while the lattice part  $\kappa_{ph}$  was modeled by experimental data from literature. The functional behaviour  $\kappa_{tot}(T)$  can be found in the original publication Ref. [44]. Adapted with permission from Ref. [44], Copyright (2012) APS.

expected. Venkatasubramanian *et al.* argued that in the SL, due to weak confinement and near zero band offset, there is minimal anisotropy between in-plane and cross-plane electrical conductivities [5]. Venkatasubramanian *et al.* concludes that in bulk  $\text{Bi}_2\text{Te}_3$  and  $\text{Sb}_2\text{Te}_3$   $\sigma_{\parallel}/\sigma_{\perp}$  is equal to 1 since the band offsets in bulk materials are zero by definition. As has been shown by our combined computational and experimental approaches [44], the latter conclusion cannot be confirmed. While in [44] we confirmed that the valence band offset is almost vanishing in all discussed SL, leading to a bulk-like behaviour (cf. Fig. 6(b)), strong quantum-well effects were found upon electron doping. Here, the electrons tend to localize in  $\text{Bi}_2\text{Te}_3$  layers, leading to a diminished cross-plane transport (cf. Figs. 6(a,c,d)). The in-plane transport properties, especially under hole doping, only showed a weak dependence on the SL period. However, no enhancement of the in-plane TE transport was found under quantum confinement, as suggested within the concept of HICKS & DRESSELHAUS. As an additional result, the LORENZ function

of the  $\text{Bi}_2\text{Te}_3/\text{Sb}_2\text{Te}_3$  SL and their directional anisotropy were found to be an intricate function of the SL period [46, 44]. Large deviations from the metallic limit  $L_0$  are evident even in the case of large extrinsic charge carrier concentrations, e.g.  $L_{\perp}/L_0 \sim 2$ . The latter finding could be important for the community, as usually the lattice thermal conductivity is derived by  $\kappa_{ph} = \kappa - L\sigma T$ . With  $\kappa$  being directly measured by  $3\omega$  methods [79], assuming too small or large LORENZ numbers leads to wrong estimations for the lattice part of the thermal conductivity [80].

Concluding, for all  $\text{Bi}_2\text{Te}_3/\text{Sb}_2\text{Te}_3$  SLs enhancements of the electronic TE transport properties could not be found. At its best, they behave as being bulk-like, and the enhancement for the figure of merit stems solely from a reduction of the cross-plane thermal conductivity. As shown in Fig. 6 and discussed in [44],  $ZT \approx 1$  for the *p*-type SL at 300 K; it reaches maximal values of  $ZT \approx 1.3$  at 450 K for the  $5\text{\AA}$   $\text{Bi}_2\text{Te}_3/10\text{\AA}$   $\text{Sb}_2\text{Te}_3$ -SL. The latter is the same SL composition for which the largest values of  $ZT$  were achieved in experiment, too [29]. While our absolute values for  $ZT$  are in contrast to the experimental findings of Venkatasubramanian *et al.*, due to the fact that the measured  $\sigma_{\parallel}/\sigma_{\perp} \approx 1$  could not be confirmed, we find very good accordance to recent experimental findings in the group of BÖTTNER *et al.* [13–15].

**4 Silicon/Germanium heterostructures** Silicon based materials are particularly interesting for TE transport, as conventional TE are often based on environmentally harmful lead, tellurium or selenium compounds and are therefore hard to integrate in semiconductor electronics. Silicon, the cradle of modern semiconductor electronics, on the other hand is non-polluting, readily available, cheap, and perfectly integrated in the present electronics infrastructure. While silicon has been stated as an inefficient thermoelectric in the past due to its large thermal conductivity, recent experiments and theory revealed that nanostructuring could lead to thermoelectric efficiencies comparable to state-of-the-art commercial thermoelectric materials [82–86].

For successful applications, an optimization of TE electronic properties of silicon, i.e. the power factor, is of utmost interest. Interfacial strain plays an important role in today's silicon-based semiconductor materials. The strain-induced enhancement of the mobility, for either electrons or holes, by strain-engineering is widely applied [87–89]. The question whether a significant enhancement of the anisotropic TE transport is achievable by biaxial strain was answered by us within publications [81] and [90]. Two directions of strain were discussed, i.e. [001]-biaxial strain [81] and [111]-biaxial strain [90]. Both alter the *n*-type TE transport due to different physical mechanisms. As shown in Figs. 7(a)-(c), in the case of [001] strain the six-fold electron pocket degeneracy is lifted and a redistribution of states into other areas of the BZ is obtained. These areas are related to other effective masses and FERMI veloci-

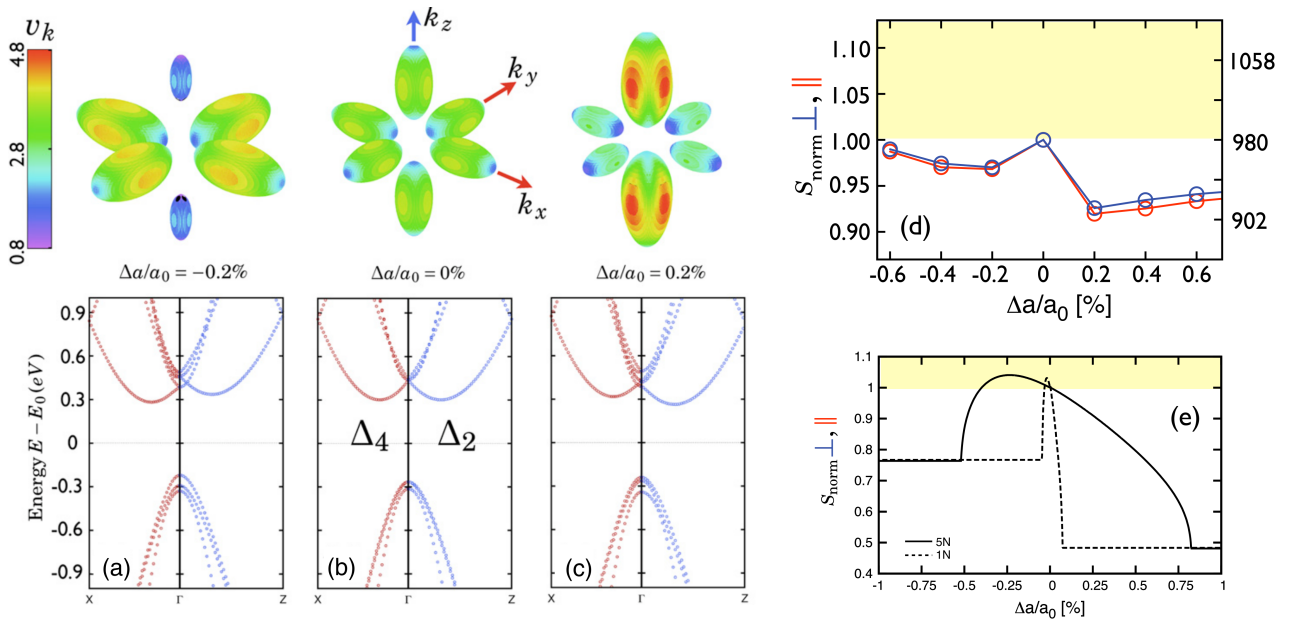


**Figure 7** FERMI surfaces of electron-doped silicon under (a) compressive strain, (b) no strain, and (c) tensile strain in [001]-direction. The absolute value of the group velocities in units of  $0.08 \times 10^6 \text{ ms}^{-1}$  are plotted on the FERMI surfaces. As a reference the band structure on two high-symmetry lines is given below. The doping corresponds to additional 0.01 electrons per unit cell which causes carrier densities of  $N = 6.25 \times 10^{19} \text{ cm}^{-3}$ . (d) Strain-dependent anisotropic thermopower in relative units (left scale) and absolute units (in  $\mu\text{V}/\text{K}$ , right scale) for the in-plane (blue) and cross-plane (red) transport directions. The temperature was fixed to 100K and the doping amounts to  $1.6 \times 10^{-7}$  electrons per unit cell. (e) Analytical dependence of the thermopower on [001]-biaxial strain for different electron charge carrier concentrations, small charge carrier concentration (dashed lines) and increased charge carrier concentration by a factor of five (solid lines). Adapted from Ref. [81]. Copyright IOP Publishing. Reproduced with permission. All rights reserved.

ties. The gain in the electrical conductivity, which can be obtained by the strain-induced redistribution of states is noticeable. However, the lifting of degeneracy was found to lead to a reduction of the thermopower (cf. Fig. 7(d)). As shown in an analytical model [81], which assumes a lifting of degenerated bands, the absolute value of the thermopower depends directly on the number of carrier pockets being occupied. As discussed in [81], the enhancement obtained in the electrical conductivity is therefore compensated by a reduction in the thermopower, leading to negligible optimization of the power factor. This picture holds over a broad temperature and doping range.

In the case of biaxial strain applied in the [111]-direction the situation is different. Here the six-fold degeneracy of the electron carrier pockets is maintained by symmetry. Contrary to the case of [001]-strain, the directional electron effective masses change with applied strain [90]. This is shown in Fig. 8(a). Due to the retained degeneracy of bands, the thermopower is less sensitive upon applied [111]-strain. It was found that the thermopower changes proportional to the change in the direction averaged effective mass (cf. inset in Fig. 8(a)), but does not drop immediately upon applying strain [90]. Summarizing, at low temperature and low doping an enhancement

of the power factor was obtained for compressive and tensile strain in the electron-doped case and for compressive strain in the hole-doped case. For the thermoelectrically more relevant high-temperature and high-doping regime a slight enhancement of the power factor was only found under small compressive strain with the power factor overall being robust against applied strain [90].

Based upon the previous findings, the TE transport of an archetypical non-symmetrized Si/Ge SL grown on Si-[111] was studied in [90]. Similar to the case of  $\text{Bi}_2\text{Te}_3/\text{Sb}_2\text{Te}_3$  SLs an evident reduction of the lattice thermal conductivity was found in Si/Ge based SL and lead to focussed experimental research [18–20]. At a first glance it was shown that no degradation of the electronic transport by the heterostructure is expected for electron doping, while even showing an enhancement of about 10% for the cross-plane power factor compared to bulk Si (cf. right scale in Fig. 8(c)). As shown in Fig. 8(b), assuming a decrease in lattice thermal conductivity, large enhancements in  $ZT$  to 0.2 and 1.4 are achieved at 300 K and 900 K, respectively. However, the predictions of an in-plane  $ZT \sim 1$  at room temperature stated by KOGA [91] could not be confirmed. Here, they used parabolic band models neglecting any coupling of adjacent layers, a

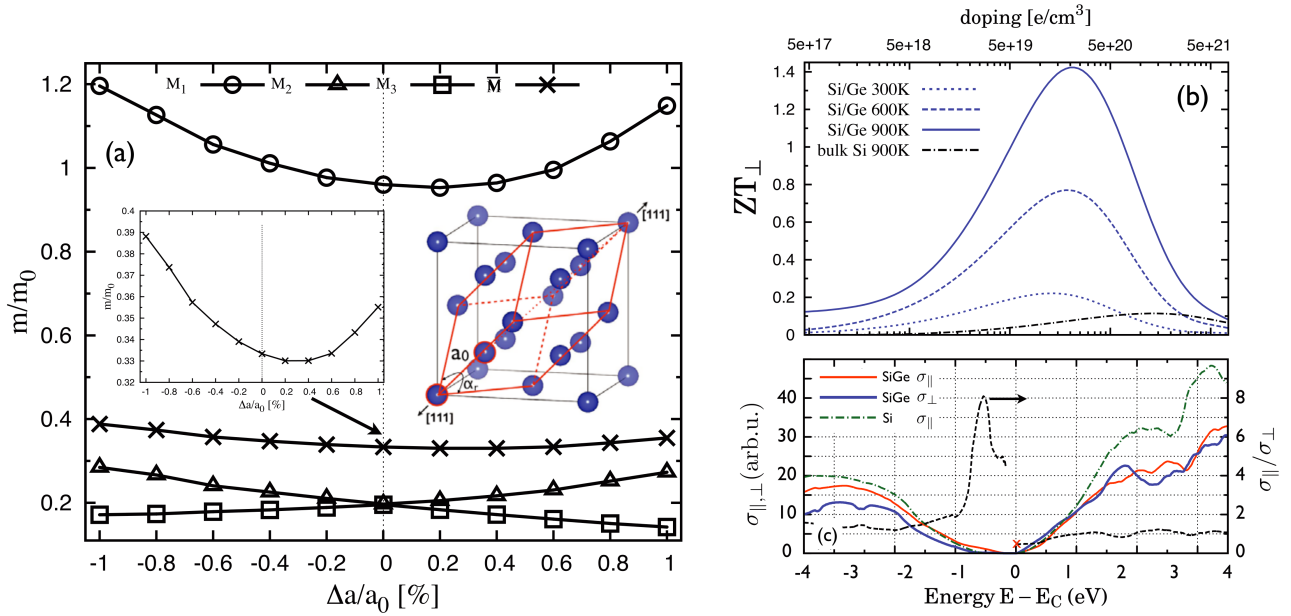


**Figure 8** (a) Directional effective conduction band masses for silicon under [111]-strain. The insets show in detail the response of the averaged effective mass  $\bar{M}$  on the applied strain, as well as the rhombohedral unit cell (red lines). (b) The doping-dependent cross-plane figures of merit  $ZT$  (of the Si/Ge-SL (blue lines) and bulk Si (black lines) under electron doping at different temperatures. (c) The electrical conductivity in dependence on the position of the chemical potential  $\mu$  at zero temperature, shown for bulk silicon (green dashed-dotted line) and the Si/Ge-SL in the in-plane (red solid line) and cross-plane (blue solid line) directions. The conductivity anisotropy (black dashed line referring to the right axis) is stated for the Si/Ge-SL. The cross at the CBM is the value obtained from an analytical effective mass approach. For the determination of the cross-plane figures of merit, the electronic part  $\kappa_{el}$  was calculated, while the lattice part  $\kappa_{ph}$  was modeled by experimental data from literature. The functional behaviour  $\kappa_{tot}(n)$  can be found in the original publication Ref. [90]. Adapted from Ref. [90]. Copyright IOP Publishing. Reproduced with permission. All rights reserved.

rather crude assumption. The results of their experimental proof-of-principle for [001]-oriented Si/Ge SL [92], showing up  $ZT \sim 0.1$  at 300K, are in closer agreement to our first-principles calculations presented in [90].

Under hole doping the electronic transport in the Si/Ge-SL is heavily suppressed due to quantum-well effects. As shown in Fig. 8(c) the electrical conductivity anisotropy is considerably increased to values of  $\sigma_{\parallel}/\sigma_{\perp} \approx 8$  at thermoelectric relevant hole doping concentrations. The valence states in a broad range around the band gap are formed by germanium states. Consequently, the *p*-type Si/Ge heterostructure consists of electrical high conducting (Ge) and nearly insulating (Si) material layers. As a result, the cross-plane power factor shows only around 50% of the bulk maximal value, leading to very small  $ZT$  values under hole doping.

**5 Summary and outlook** During the period of the Priority Program SPP 1386 we developed a method to fully describe the thermoelectric properties in the diffusive limit of transport for three-dimensional bulk systems and their two-dimensional partners, i.e. heterostructures and thin films, on a consistent and convenient *ab initio* foot-

ing. While fundamentals of the functionality of phonon-blocking and electron-transmitting superlattices could be unveiled, we provided also distinct analysis and ideas for TE enhancement for the two archetypical TE heterostructures based on  $\text{Bi}_2\text{Te}_3/\text{Sb}_2\text{Te}_3$  and Si/Ge.

Summarizing, the interdependence of the thermoelectric transport properties remains a big obstacle in thermoelectric superlattices and bulk materials. Optimizing the electronic transport properties by tuning the charge carrier concentration seems to remain the only efficient and promising approach.

As an alternative *ansatz* it was suggested to enhance the thermoelectric transport by strain, or in other words, to understand whether strain could be the reason for enhanced cross-plane thermoelectric transport, even at the expense of a possibly less efficient in-plane transport. In both material systems, no pronounced enhancement could be found, while the transport properties were robust against strain, especially in the thermoelectric desirable high-doping and high-temperature regime. While for  $\text{Bi}_2\text{Te}_3$  a decrease of the maximal power factor of about 27% and 23% for *n* and *p*-doping, respectively, was found, the strain shows nearly no influence on the power factor for  $\text{Sb}_2\text{Te}_3$ .

For Si/Ge-based superlattices, strain along the [111]-direction was found to be preferable with respect to [001]-strain. Under biaxial strain in [001]-direction lifting of the band's degeneracy causes reoccupation of states in the BRILLOUIN zone, which can enhance the electrical conductivity in some cases, but is always related to a decrease of the thermopower. Both effects tend to compensate each other. The degeneracy of the conduction bands is preserved by symmetry in the case of strain along the [111]-direction. Therefore, a reduction of the thermopower is not expected *a priori*.

The studies on the thermoelectric transport of the superlattices revealed distinct similarities, too. For both superlattice systems, the band gap differences between the bulk materials caused band offsets in the heterostructures. These band offsets tend to localize entirely at either the valence band edge or the conduction band edge, causing strong quantum confinement effects of the carriers in the cross-plane transport direction. For  $\text{Bi}_2\text{Te}_3/\text{Sb}_2\text{Te}_3$  SLs, quantum confinement leads to a strong reduction of the cross-plane transport under *n*-doping, while for the Si/Ge superlattice the *p*-type transport was diminished. The complementary *n* or *p*-type transport properties were found to be bulk-like, or could only be slightly enhanced, as shown for the Si/Ge superlattice. The remarkable experimental findings of a strongly enhanced cross-plane transport in the  $\text{Bi}_2\text{Te}_3/\text{Sb}_2\text{Te}_3$  SLs could not be confirmed.

Nevertheless, for at least one carrier-type (electron or hole transport) bulk-like electronic transport can be expected in thermoelectric superlattices, enabling to benefit from the reduction of the lattice thermal conductivity for an enhanced figure of merit.

Further studies could account additionally for interfacial disorder or the detailed influence of scattering effects, like electron-impurity, phonon-phonon and electron-phonon scattering, to get more insight into the complexity of thermoelectric heterostructures.

## References

- [1] M. Gradhand, M. Czerner, D. V. Fedorov, P. Zahn, B. Y. Yavorsky, L. Szunyogh, and I. Mertig, *Physical Review B* **80**(22), 224413 (2009).
- [2] P. Giannozzi and many others, *J. Phys.: Condens. Matter* **21**, 395502 (2009).
- [3] G. Kresse and J. Furthmüller, *Phys. Rev. B* **54**, 11169–11186 (1996).
- [4] R. Venkatasubramanian, T. Colpitts, B. O'Quinn, S. Liu, N. El-Masry, and M. Lamvik, *Applied Physics Letters* **75**(8), 1104–1106 (1999).
- [5] R. Venkatasubramanian, E. Siivola, and T. Colpitts, *Nature* **413**, 597 (2001).
- [6] G. Slack (Academic Press, New York, 1979), pp. 1–71.
- [7] G. A. Slack, (CRC Press, Boca Raton, 1995), chap. 34, , 701.
- [8] L. Hicks and M. Dresselhaus, *Physical Review B* **47**(19), 12727–12731 (1993).
- [9] L. Hicks, T. Harman, X. Sun, and M. Dresselhaus, *Physical Review B* **53**(16), R10493–R10496 (1996).
- [10] H. Böttner, G. Chen, and R. Venkatasubramanian, *MRS bulletin* **31**(3), 211 (2006).
- [11] R. Venkatasubramanian, T. Colpitts, E. Watko, M. Lamvik, and N. El-Masry, *Journal of crystal growth* **170**(1-4), 817–821 (1997).
- [12] M. N. Touzelbaev, P. Zhou, R. Venkatasubramanian, and K. E. Goodson, *Journal of Applied Physics* **90**(2), 763 (2001).
- [13] J. König, M. Winkler, S. Buller, W. Bensch, U. Schürmann, L. Kienle, and H. Böttner, *Journal of Electronic Materials* **40**(5), 1266 (2011).
- [14] M. Winkler, X. Liu, J. D. König, L. Kirste, H. Böttner, W. Bensch, and L. Kienle, *Journal of Electronic Materials* **41**(6), 1322 (2011).
- [15] M. Winkler, X. Liu, J. D. König, S. Buller, U. Schürmann, L. Kienle, W. Bensch, and H. Böttner, *J. Mater. Chem.* **22**(22), 11323–11334 (2012).
- [16] R. Venkatasubramanian, T. Colpitts, E. Watko, and J. Hutchby, *Proceedings of the XV International Conference on Thermoelectrics* pp. 454–458 (1996).
- [17] R. Venkatasubramanian, *Naval Research Reviews, Special Issue on Thermoelectric* (1997).
- [18] S. Lee, D. Cahill, and R. Venkatasubramanian, *Appl. Phys. Lett.* **70**(22), 2957 (1997).
- [19] T. Borca-Tasciuc, *Superlattices and Microstructures* **28**(3), 199–206 (2000).
- [20] B. Yang, J. Liu, K. Wang, and G. Chen, *Proceedings of the XX International Conference on Thermoelectrics* pp. 344–347 (2001).
- [21] T. C. Harman, P. J. Taylor, D. L. Spears, and M. P. Walsh, *Journal of Electronic Materials* **29**(1), L1–L2 (2000).
- [22] T. Harman, P. Taylor, M. Walsh, and B. LaForge, *Science* **297**(5590), 2229 (2002).
- [23] T. C. Harman, M. P. Walsh, B. E. Laforge, and G. W. Turner, *Journal of Electronic Materials* **34**(5), L19–L22 (2005).
- [24] H. Beyer, J. Nurnus, H. Böttner, A. Lambrecht, T. Roch, and G. Bauer, *Applied Physics Letters* **80**(7), 1216 (2002).
- [25] H. Beyer, J. Nurnus, H. Böttner, A. Lambrecht, E. Wagner, and G. Bauer, *Physica E: Low-dimensional Systems and Nanostructures* **13**(2-4), 965–968 (2002).
- [26] J. Jeffers, K. Namjou, Z. Cai, P. McCann, and L. Olona, *Applied Physics Letters* **99**(4), 041903 (2011).
- [27] S. Cho, Y. Kim, S. Youn, A. DiVenere, and G. Wong, *Physical Review B* **64**(23), 235330 (2001).
- [28] J. Caylor, M. Sander, A. Stacy, J. Harper, R. Gronsky, and T. Sands, *Journal of Materials Research* **16**(9), 2467 (2001).
- [29] R. Venkatasubramanian, *Physical Review B* **61**(4), 3091–3097 (2000).
- [30] S. Chakraborty, C. Kleint, A. Heinrich, C. Schneider, J. Schumann, M. Falke, and S. Teichert, *Applied Physics Letters* **83**, 4184 (2003).
- [31] S. Huxtable, A. Abramson, and C. Tien, *Applied Physics Letters* **80**(10), 1737 (2002).
- [32] Y. Ezzahri, S. Grauby, J. Rampnoux, H. Michel, G. Perrot, W. Claeys, S. Dilhaire, C. Rossignol, G. Zeng, and A. Shakouri, *Physical Review B* **75**(19), 195309 (2007).

- [33] G. Chen, *Physical Review B* **57**(23), 14958 (1998).
- [34] P. Hyltdgaard and G. Mahan, *Physical Review-Section B-Condensed Matter* **56**(17), 10754–10757 (1997).
- [35] S. Tamura, Y. Tanaka, and H. Maris, *Physical Review B* **60**(4), 2627 (1999).
- [36] C. Vineis, T. Harman, S. Calawa, M. Walsh, R. Reeder, R. Singh, and A. Shakouri, *Physical Review B* **77**(23), 235202 (2008).
- [37] J. M. Ziman, *Electrons and phonons* (Clarendon Press, Oxford, 1960).
- [38] I. Mertig, *Reports on Progress in Physics* **62**, 237 (1999).
- [39] G. Mahan and J. O. Sofo, *PNAS* **93**(15), 7436 (1996).
- [40] M. Stordeur and W. Kühnberger, *Physica status solidi (b)* **69**(2), 377–387 (1975).
- [41] H. Kaibe, *Journal of Physics and Chemistry of Solids* **50**(9), 945–950 (1989).
- [42] H. Goldsmid, *Advances in Physics* **14**(55), 273 (1965).
- [43] N. F. Hinsche, B. Y. Yavorsky, I. Mertig, and P. Zahn, *Physical Review B* **84**(16), 165214 (2011).
- [44] N. F. Hinsche et al., *Physical Review B* **86**(8), 085323 (2012).
- [45] G. Nolas and H. Goldsmid, *Thermal Conductivity of Semiconductors*, (Kluwer Academic, New York, 2004), chap. 1.4.
- [46] N. Hinsche, I. Mertig, and P. Zahn, *Journal of Electronic Materials* (2012).
- [47] C. Goupil, W. Seifert, K. Zabrocki, E. Müller, and G. Snyder, *Entropy* **13**(8), 1481–1517 (2011).
- [48] G. Snyder, E. Toberer, R. Khanna, and W. Seifert, *Physical Review B* **86**(4), 045202 (2012).
- [49] W. Seifert, G. Snyder, E. Toberer, C. Goupil, K. Zabrocki, and E. Müller, *Physica Status Solidi A* **210**, 1407–1417 (2013).
- [50] J. Lee, M. Asheghi, and K. E. Goodson, *Nanotechnology* **23**(20), 5201 (2012).
- [51] J. Callaway, *Physical Review* **113**(4), 1046–1051 (1959).
- [52] R. Guyer and J. Krumhansl, *Physical Review* **148**(2), 766–778 (1966).
- [53] H. Smith and H. H. Jensen (Clarendon Press, Oxford, 1989).
- [54] H. Rauh, H. K. R. Geick, N. Nücker, and N. Lehner, *J. Phys. C* **14**, 2705–2712 (1981).
- [55] D. Bessas, I. Sergueev, H. Wille, J. Persson, D. Ebling, and R. P. Hermann, *Phys. Rev. B* **86**, 224301 (2012).
- [56] G. Kresse and D. Joubert, *Phys. Rev. B* **58**, 1758–1775 (1999).
- [57] M. Schackert, T. Markl, J. Jandke, M. Holzer, S. Ostanin, E. K. U. Gross, A. Ernst, and W. Wulfhekel, *Phys. Rev. Lett.* **114**(4) (2015).
- [58] J. O. Jenkins, R. W. Ure, and J. A. Rayne, *Phys. Rev. B* **5**, 3171 (1972).
- [59] P. Allen, *Physical Review B* **88**(14) (2013).
- [60] J. Ma, W. Li, and X. Luo, *Physical Review B* **90**(1), 035203 (2014).
- [61] S. Shindé and G. Srivastava (Springer, 2014).
- [62] A. Debernardi, S. Baroni, and E. Molinari, *Phys. Rev. Lett.* **75**(9), 1819–1822 (1995).
- [63] K. Esfarjani and H. Stokes, *Physical Review B* **77**(14), 144112 (2008).
- [64] A. Ward and D. A. Broido, *Physical Review B* **81**(8), 085205 (2010).
- [65] G. Deinzer, G. Birner, and D. Strauch, *Physical Review B* **67**(14), 144304 (2003).
- [66] A. Ward, D. Broido, D. Stewart, and G. Deinzer, *Physical Review B* **80**(12), 125203 (2009).
- [67] O. Hellman and D. Broido, *Physical Review B*.
- [68] J. Garg, N. Bonini, and N. Marzari, *Nano Letter* **11**(12), 5135 (2011).
- [69] J. Garg and G. Chen, *Phys. Rev. B* **87**, 140302 (2013).
- [70] W. Li, J. Carrete, N. Katcho, and N. Mingo, *Computer Physics Communications* **185**(6), 1747 (2014).
- [71] H. Goldsmid, A. Sheard, and D. Wright, *British Journal of Applied Physics* **9**(9), 365 (1958).
- [72] D. A. Wright **181**(4612), 834 (1958).
- [73] B. Poudel, Q. Hao, Y. Ma, Y. Lan, A. Minnich, B. Yu, X. Yan, D. Wang, A. Muto, and D. Vashaee, *Science* **320**(5876), 634 (2008).
- [74] B. Y. Yavorsky, N. F. Hinsche, I. Mertig, and P. Zahn, *Physical Review B* **84**(16), 165208 (2011).
- [75] J. R. Drabble, R. D. Groves, and R. Wolfe, *Proceedings of the Physical Society* **71**(3), 430 (1958).
- [76] P. Zahn, N. F. Hinsche, B. Y. Yavorsky, and I. Mertig, *J. Phys.: Condens. Matter* **23**, 505504 (2011).
- [77] M. Stordeur and W. Heiliger, *Physica status solidi (b)* **78**(2), K103–K106 (1976).
- [78] M. Stordeur, *Physica status solidi (b)* **98**(1), 199–206 (1980).
- [79] T. Borca-Tasciuc, A. Kumar, and G. Chen, *Rev. Sci. Instrum.* **72**(4), 2139 (2001).
- [80] J. Sharp, E. Volckmann, and H. Goldsmid, *Physica status solidi (a)* **185**(2), 257–265 (2001).
- [81] N. F. Hinsche, I. Mertig, and P. Zahn, *J. Phys.: Condens. Matter* **23**, 295502 (2011).
- [82] C. B. Vining, *Nature* **451**(7175), 132–133 (2008).
- [83] R. Chen, A. I. Hochbaum, P. Murphy, J. Moore, P. Yang, and A. Majumdar, *Physical Review Letters* **101**(10), 105501 (2008).
- [84] A. Hochbaum, R. Chen, R. Delgado, and W. Liang, *Nature* **451**(7175), 163 (2008).
- [85] S. K. Bux, R. G. Blair, P. K. Gogna, H. Lee, G. Chen, M. S. Dresselhaus, R. B. Kaner, and J. P. Fleurial, *Adv. Funct. Mater.* **19**(15), 2445–2452 (2009).
- [86] J. Boor, D. S. Kim, X. Ao, M. Becker, N. F. Hinsche, I. Mertig, P. Zahn, and V. Schmidt, *Appl. Phys. A* **107**(4), 789–794 (2012).
- [87] M. Fischetti and S. Laux, *Journal of Applied Physics* **80**(4), 2234–2252 (1996).
- [88] T. Dziekan, P. Zahn, V. Meded, and S. Mirbt, *Physical Review B* **75**(19), 195213 (2007).
- [89] M. O. Baykan, S. E. Thompson, and T. Nishida, *Journal of Applied Physics* **108**(9), 093716 (2010).
- [90] N. F. Hinsche, I. Mertig, and P. Zahn, *J. Phys.: Condens. Matter* **24**(27), 275501 (2012).
- [91] T. Koga, X. Sun, S. Cronin, and M. Dresselhaus, *Applied Physics Letters* **75**, 2438 (1999).
- [92] T. Koga, S. Cronin, M. Dresselhaus, and J. Liu, *Applied Physics Letters* **77**(10), 1490 (2000).